Bandwidths and amplitudes of chorus-like banded emissions measured by the TC-1 Double Star spacecraft

E. Macusova, O. Santolík, Nicole Cornilleau-Wehrlin, K. H. Yearby

AGU PUBLICATIONS

JGR

Journal of Geophysical Research: Space Physics

RESEARCH ARTICLE

10.1002/2014JA020440

Key Points:
- New analysis method based on determination of bandwidths of chorus-like waves
- TC-1 data show that the lower band has 3 times larger amplitudes than the upper band
- Most intense emissions were found close to the equator at L<10 and at MLT 22–09 h

Correspondence to:
E. Macúšová,
em@ufa.cas.cz

Citation:
Macúšová, E., O. Santolík, N. Cornilleau-Wehrlin, and K. H. Yearby (2015), Bandwidths and amplitudes of chorus-like banded emissions measured by the TC-1 *Double Star* spacecraft, *J. Geophys. Res. Space Physics*, *120*, 1057–1071, doi:10.1002/2014JA020440.

Received 25 JUL 2014
Accepted 6 JAN 2015
Accepted article online 11 JAN 2015
Published online 7 FEB 2015

Bandwidths and amplitudes of chorus-like banded emissions measured by the TC-1 *Double Star* spacecraft

E. Macúšová[1], O. Santolík[1,2], N. Cornilleau-Wehrlin[3,4], and K. H. Yearby[5]

[1]Institute of Atmospheric Physics, Prague, Czech Republic, [2]Faculty of Mathematics and Physics, Charles University, Prague, Czech Republic, [3]LPPP/CNRS-Ecole Polytechnique, Palaiseau, France, [4]LESIA, Observatoire de Paris, Meudon, France, [5]Department of Automatic Control and Systems Engineering, University of Sheffield, Sheffield, England

Abstract Characteristics of banded whistler-mode emissions are derived from a database of chorus-like events obtained from the complete data set of the wave measurements provided by the Spatio-Temporal Analysis of Field Fluctuation-Digital Wave Processing (STAFF-DWP) wave instrument on board the TC-1 *Double Star* spacecraft. Our study covers the full operational period of this spacecraft (almost 4 years). Our entire data set has been collected within 30° of geomagnetic latitude at L shells between 2 and 12 and below 4 kHz. All events have been processed automatically to accurately determine their power spectral density (PSD), bandwidth, and amplitude. We found most cases of chorus-like banded emissions at $L \leq 10$ on the dawnside and dayside. The upper band emissions (above one half of the equatorial electron cyclotron frequency) occur almost 20 times less often than the lower band, and their average amplitude is almost 3 times smaller than for the lower band. Intense upper band emissions cover smaller L shell, magnetic local time (MLT), and magnetic latitudes regions than intense lower band emissions. The intense nightside and dawnside chorus-like banded emissions were observed at low magnetic latitudes, while the intense dayside and duskside emissions were mostly found at higher magnetic latitudes. The amplitudes of dayside lower band waves slightly increase as they propagate away from the geomagnetic equator and are smaller than chorus amplitudes on nightside and dawnside. The PSD, the amplitude of the lower band, its frequency bandwidth, and its occurrence rate significantly increase with increasing geomagnetic activity, while all these parameters for the upper band are not so strongly dependent on the geomagnetic activity.

1. Introduction

Whistler-mode chorus waves are natural electromagnetic emissions observed outside the plasmapause. They are believed to be generated in the geomagnetic equatorial region by cyclotron resonant interactions with suprathermal electrons [*Katoh and Omura*, 2007]. They propagate from the geomagnetic equator toward larger magnetic latitudes [*Santolik and Gurnett*, 2003; *Sazhin and Hayakawa*, 1992].

LeDocq et al. [1998], *Parrot et al.* [2003], *Santolik and Gurnett* [2003], and *Santolik et al.* [2005a] found from the Poynting flux measurements that the source region is located within a few degrees from the geomagnetic equator, and its size varied from 3000 to 5000 km along the geomagnetic field lines. In these observations, the source region of the chorus emissions was spread over L shells from 4 to 5. Chorus at L up to 9 has been found from the first *Double Star* (TC-1) measurements by *Santolik et al.* [2005b]. Extension of previous chorus observations beyond $L \sim 7$ to $L \sim 13$ has been shown from Time History of Events and Macroscale Interactions during Substorms (THEMIS) measurements by *Li et al.* [2009] and from multisatellite measurements by *Meredith et al.* [2012].

Chorus emissions located close to the geomagnetic equator often occur over the frequency range f_{lh}–f_{ce} [*Tsurutani and Smith*, 1977], where f_{lh} is the lower hybrid frequency and f_{ce} is the electron cyclotron frequency. They also often exhibit two frequency bands (the lower and the upper band) separated by a gap localized near 0.5 f_{ce} [*Tsurutani and Smith*, 1974]. But in some case studies, individual chorus elements crossing the region of 0.5 f_{ce} are also observed [*Burtis and Helliwell*, 1976; *Cornilleau-Wehrlin et al.*, 1978; *Kurita et al.*, 2012].

Santolik et al. [2005b] have found that the upper band chorus is confined to lower L shells (< 8) and lower magnetic latitudes ($|\lambda_m| < 10°$) in comparison with the lower band chorus occurring in a wider range of λ_m (geomagnetic latitude) and L shells, as well as in a wider magnetic local time (MLT) interval. *Li et al.* [2011b]

confirmed these results. They studied how the distributions of chorus bands depend on the MLT, L shell, and λ_m and found that the wave normal angles of upper band chorus are larger than those of lower band chorus. *Meredith et al.* [2012] have used, for a similar study, extended source of data from five satellite missions and have seen the equatorial chorus ($|\lambda_m| < 15°$) with intensities of the order 2000 pT^2 between 23 and 12 MLT and intense middle-latitude chorus ($15° > |\lambda_m| > 30°$) on the dayside MLT (7–14). In both cases, emissions with maximum intensities were found during active conditions at L^* from 4 to 7. Previous studies by *Tsurutani and Smith* [1977] and *Li et al.* [2009] have shown that nightside chorus waves are confined within 15° of the magnetic equator, whereas dayside chorus waves extend to higher magnetic latitudes. This is also in agreement with the results of *Meredith et al.* [2012]. The wave amplitude is closely connected with properties of ambient magnetic field and ambient plasma environment. It means that emissions have the largest intensities during active conditions [*Meredith et al.*, 2012].

The intensity of chorus is increasing by a nonlinear growth mechanism [*Omura et al.*, 2009; *Li et al.*, 2011a; *Katoh and Omura*, 2011; *Tao et al.*, 2012]. The work of *Haque et al.* [2012] based on 12 different Cluster orbits has shown that the intensity of chorus emissions increases exponentially with the increasing distance from the magnetic equator. It quantitatively agrees with numerical simulation of *Omura et al.* [2009] and *Katoh and Omura* [2011].

Whistler-mode chorus frequency bands consist predominantly of discrete rising tones, short impulsive bursts [*Burtis and Helliwell*, 1969], but falling tones, constant frequency tones, and hooks were also observed [*Burtis and Helliwell*, 1976]. *Li et al.* [2011a, 2011b] have shown that rising tones are more quasi-field aligned, that they usually occur from the midnight to the afternoon MLT hours, and that they have larger amplitudes than those of falling tones. The falling tones are usually more oblique and propagate close to the resonant cone, as it was previously indicated by a case study of *Santolik et al.* [2009]. They are observed between local midnight and noon. *Li et al.* [2011a] suggested that two different mechanisms may be responsible for generation of rising and falling tones. They found that large amplitude chorus waves are preferentially observed at lower magnetic latitudes ($|\lambda_m| < 10°$) from premidnight to postdawn MLT.

Whistler mode chorus primarily affects the dynamics of the outer radiation belt electrons [*Thorne et al.*, 2013], but it has been also shown that chorus emissions may also play an important role in the generation of plasmaspheric hiss [*Chum and Santolík*, 2005; *Santolik et al.*, 2006; *Bortnik et al.*, 2008; *Chen et al.*, 2012a, 2012b]. Chorus waves can also scatter plasma sheet electrons with energies from a few hundreds of eV to a few tens of keV into the atmosphere and form there the diffuse or pulsating auroras [*Thorne et al.*, 2010; *Ni et al.*, 2008; *Nishimura et al.*, 2010].

In our study we concentrate on analysis of the lower and upper bands of whistler-mode banded emissions, their power spectral densities (PSD), frequency bandwidths (BW), amplitudes, and occurrence rates. The time resolution of our measurements is 4 s. We are therefore unable to distinguish whether the observed emissions have a typical discrete structure of chorus or if they have a form of hiss, and we describe all of them as chorus-like emissions. The absolute amplitudes of fluctuating magnetic fields were approximately estimated based on measured power spectral densities and assumed bandwidths in previous papers, for instance in studies of *Li et al.* [2011a] and *Meredith et al.* [2012]. We calculated the amplitude from detected bandwidths of emissions and from their PSD. We use measurements of the *Double Star* TC-1 equatorial satellite as the source of data. The TC-1 orbits covered a wide L shell interval in the chorus source region. We use the entire operational period of the spacecraft corresponding to the almost 4 years of measurements. This gives us an opportunity to study properties of chorus-like banded emissions and their variations under different geomagnetic conditions and in different regions of the Earth's magnetosphere. The *Double Star* mission and the procedure of data processing are briefly described and summarized in sections 2 and 3. Results of a statistical survey are described in section 4 and discussed in section 5. The main conclusions are summarized in section 6.

2. The Data Set

The *Double Star* mission consisted of two satellites [*Escoubet et al.*, 2005]. The first satellite, TC-1, had an eccentric equatorial elliptical orbit of 570 × 78, 970 km, inclined at 28.5° with respect to the equator. The second spacecraft, TC-2, orbited in a polar plane with an apogee of 39,000 km and a perigee of 700 km. The TC-1 spacecraft operated from the end of December 2003 till the end of September 2007, and its orbit

permits the investigation of the chorus source region close to the geomagnetic equatorial plane in a wide interval of L shells and in all MLT sectors.

The equatorial satellite TC-1 carried eight particle and field instruments. Four of them were provided by ESA and were identical to those on board the four Cluster spacecraft. We primarily use the Spatio-Temporal Analysis of Field Fluctuation-Digital Wave Processing (STAFF-DWP) wave instrument which consists of a combination of two instruments, the Spatio-Temporal Analysis of Field Fluctuation (STAFF) experiment and the Digital Wave Processing (DWP) experiment [*Cornilleau-Wehrlin et al.*, 2005]. The measurements of a three-axis search coil magnetometer were processed by DWP in time intervals of one spin period of the spacecraft, which gives us a 4 s time resolution. That limited our ability to determine if the chorus-like banded emissions contained discrete structures of chorus or if they had a form of a shapeless hiss. DWP computed on board fast Fourier transform and used them to form, in a given time interval of analysis, 27 spectral matrices (three power spectra and three complex cross spectra) in 27 approximately logarithmically spaced channels covering the frequency range from 10 Hz to 4 kHz. The nominal boundaries of each frequency channel are defined by the points where the amplitude response is reduced to one half (−6dB). The frequency separation between these two boundaries (full width at half maximum) represents two half widths of each channel. The half widths vary between 10 Hz and 320 Hz.

Unfortunately, the solid boom carrying the search coil magnetometer did not deploy correctly. This caused intense interferences from the spacecraft. The DWP data were therefore analyzed on the ground to minimize the interferences by selecting the optimum combination of signals from the three search coils. As a result of this processing we reduce the spectral matrix into one power spectrum with minimized interference signals. For this reason we calculated the power spectral density (PSD) of magnetic field fluctuations and the amplitude of all selected emissions only from this component of the magnetic field. The PSD values resulting from this procedure can be therefore considered as lower estimates of the true PSD values.

The absence of electric field measurements on board TC-1 caused that we were unable to determine the exact position of the source region and propagation properties by using the same methods as *Santolik et al.* [2003, 2004].

3. Processing of Chorus-Like Banded Emissions

We have first prepared a list of time intervals containing BEs (banded emissions) that were visually preselected from time-frequency spectrograms of the power spectral density (PSD) of magnetic field fluctuations and that satisfied several selection criteria. The intensity of selected banded emission had to be at least 2 orders of magnitude larger than the intensity of the background and the entire selected time interval needed to contain only chorus-like banded emissions and to be unaffected by the artificial interference [*Macúšová and Santolík*, 2009].

Examples of time-frequency spectrograms obtained from TC-1 measurements that were used for visual detection of BE are given in Figures 1a and 2a. Time intervals selected during visual inspection are marked with red rectangles. Only these time intervals are used for our statistical study. From the first red rectangle in Figure 2a it is evident that the lower cutoff of the upper frequency band corresponds quite well to half the equatorial electron cyclotron frequency (1/2 f_{ceq}). This does not necessarily mean that our observations disagree with the recent analysis of Geotail measurements by *Yagitani et al.* [2014] where the lower cutoff of the upper band that follows half the local f_{ce}: f_{ceq} is very close to f_{ce} at low magnetic latitudes of our measurements.

Black rectangles are time intervals where the selection criteria were not satisfied. The black rectangle in Figure 1a after 03:00 UT shows intense waves at frequencies below the lower hybrid frequency in the equatorial region, probably corresponding to equatorial noise. These waves, together with noise above the lower hybrid frequency, exclude this time interval from further analysis because the power spectral density of band-limited emissions does not reach 2 orders of magnitude above the background. The time interval in the first black rectangle in Figure 2a contains a strong artificial interference. It caused its exclusion from further analysis. A diffuse transition between the lower cutoff of the BE, and the background caused the disqualification of the time interval in the second black rectangle because it is difficult to determine where exactly the lower cutoff of the lower band BE is localized.

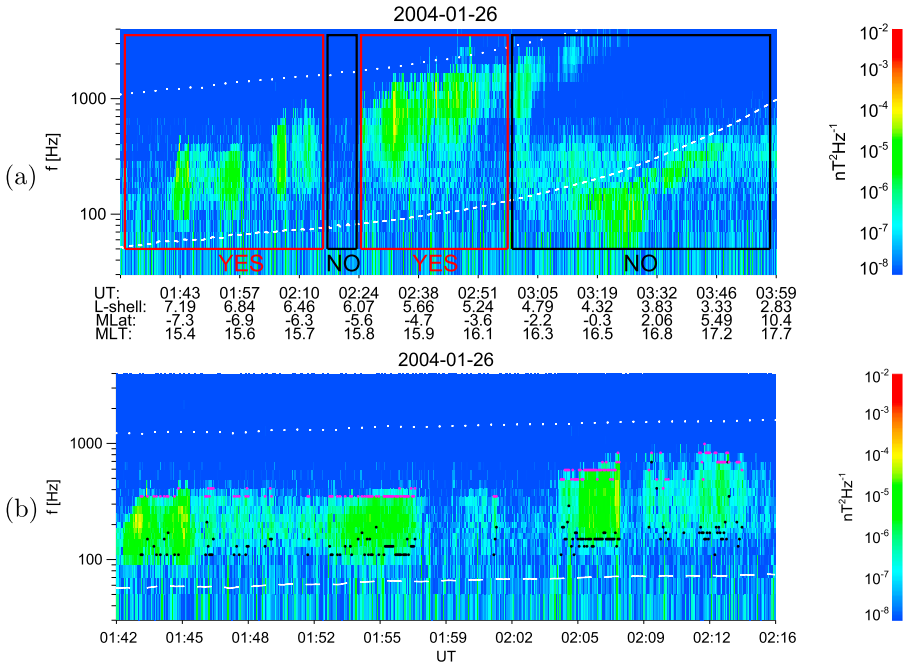

Figure 1. Power spectral density spectrograms of magnetic field fluctuations measured on 26 January 2004. (a) A 2.5 h interval from 1:30 UT shows the visually selected intervals fulfilling selection criteria that are used for further processing (red rectangles) according to the selection criteria given in the text, (b) a 34 min long subinterval (part of the first red rectangle in Figure 1a) that shows detection of the banded emission by the automatic band recognition procedure. The dotted white lines reflect half the equatorial electron cyclotron frequency $1/2f_{ceq}$, and the dashed white lines show lower hybrid frequency f_{lh}. Spacecraft position is given in Figure 1a: UT, universal time; L shell; MLat, magnetic dipole latitude; MLT, magnetic local time. Magenta dots in Figure 1b show the upper cutoff of the lower band emission and black dots show its lower cutoff.

The list of 603 selected time intervals fulfilling selection criteria and containing chorus-like banded emissions covers almost 784 h of data. These time intervals were processed by an automated procedure as follows:

1. For each time point (each 4 s time interval) we divide the 27 frequency channels into two frequency ranges: $f_{lh} \le f < 1/2f_{ceq}$ and $1/2f_{ceq} \le f < f_{ceq}$, respectively, where f_{lh} is the local lower hybrid frequency and f_{ceq} is the equatorial electron cyclotron frequency for a given time point obtained from a dipole approximation as

$$f_{ceq} = f_{ce}/\sqrt{1 + 3\sin(\lambda_m)^2}. \quad (1)$$

2. We find the frequency channel with the maximum PSD for each time point and for each of the two frequency ranges separately. The adjacent frequency channels to the channel with the maximum PSD value are also selected if they all fulfill the condition

$$p_{m+i} \ge 0.05\, p_m, \quad (2)$$

where p_j is the PSD in jth frequency channel, 0.05 is a threshold value, m corresponds to the channel with the maximum PSD, and i represents the position of the frequency channel with respect to the channel with the maximum PSD value. Min(i)= $l \le 0$ corresponds to the lowest-frequency channel from a continuous sequence fulfilling the criterion 2. Max(i)= $u \ge 0$ corresponds to the highest-frequency channel from this sequence. The threshold value has been determined based on the properties of the analyzed data set. On one hand, when we decrease the threshold the procedure will often detect also frequency channels corresponding to the background noise. On the other hand, a larger threshold narrows the bandwidth although it clearly appears larger on the spectrograms. A threshold value of 0.05 seems to be the best compromise for this particular study.

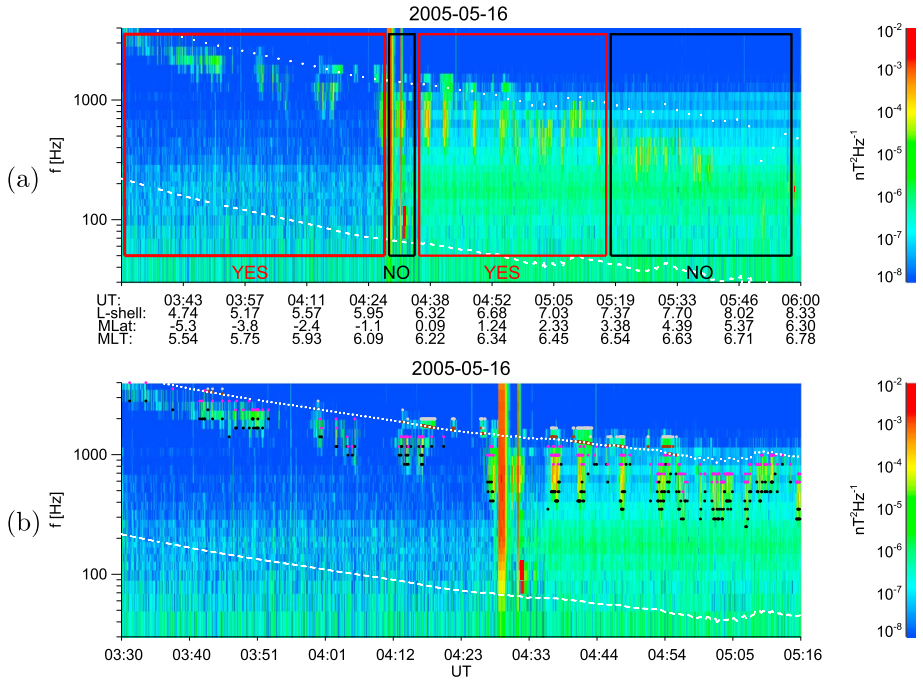

Figure 2. Power spectral density spectrograms of magnetic field fluctuations measured on 16 May 2005, the same panels as in Figure 1. (a) A 2.5 h interval from 3:30 UT showing visually selected intervals. (b) 106 min long subinterval representing the red rectangles from Figure 2a. Besides symbols already described in Figure 1, gray dots show the upper cutoff of the upper frequency band defined by an automatic band recognition procedure and brown dots represent its lower cutoff.

3. The total PSD for each time point and for each of the two frequency ranges is calculated as

$$\mathrm{PSD} = \frac{\sum_{j=m+l}^{m+u} p_j\, w_j}{\sum_{j=m+l}^{m+u} w_j}, \tag{3}$$

where $u - l + 1$ is the number of selected frequency channels that have satisfied the condition 2, p_j are values of PSD in the selected frequency channels and w_j are the frequency bandwidths of the particular selected channels.

4. The total frequency BW (Bandwidth) for each time point and for each frequency range was determined as

$$\mathrm{BW} = \sum_{j=m+l}^{m+u} w_j = F_u - F_l, \tag{4}$$

where F_u is the highest frequency among the selected frequency channels (the upper frequency limit of the channel $m+u$). F_l is the lowest frequency among the selected channels (the lower frequency limit of the channel $m+l$).

5. The amplitude A of each time point for each frequency band (lower or upper) is calculated as

$$A = \sqrt{\sum_{j=m+l}^{m+u} p_j\, w_j}. \tag{5}$$

6. Three conditions have been also checked inside time subintervals containing 100 nearest time points (6 min and 40 s):
   a. Each time point (each 4 s) from one particular time interval with the intensity close to the intensity of background of this particular time interval was excluded by the condition PSD $< 0.1\,\overline{\mathrm{PSD}}$, where $\overline{\mathrm{PSD}}$ is the average value of PSD for all time points within a given time interval. This additional condition excludes all short time subintervals that did not contain the BE. Time intervals excluded by this condition are given, for example, in Figure 1b between 01:58–02:00 UT, 02:01–02:04 UT, and 02:08–02:09 UT and in Figure 2b 03:54–04:00 UT, etc.

b. Time points with extremely low or extremely high BW were excluded by conditions BW $> 2\,\overline{\mathrm{BW}}$, BW $< \overline{\mathrm{BW}}/2$, where $\overline{\mathrm{BW}}$ is the average value of BW for all time points within a given time interval. This additional condition removes all undesirable broadband or narrowband interferences with the intensity close to the intensity of BE.

c. To prevent sudden frequency shifts of the selected band, we also exclude the time points fulfilling the condition $F_u < \overline{F_l}$, where F_u is the upper frequency limit of the selected bandwidth at a given time point and $\overline{F_l}$ is the average value of the lower frequency limits of selected bandwidths calculated from all time points within a given each subinterval of 100 nearest time points.

This condition mainly disqualifies time points with intense broadband background. An example is given in Figure 2b between 4:09 and 4:11 UT.

Two examples of output of this procedure are given in Figures 1b and 2b which, respectively, show 34 min and 106 min long time subintervals from Figures 1a and 2a. In these plots, the white dotted lines correspond to $1/2f_{ceq}$, the white dashed lines show the local f_{lh}. Values of $1/2f_{ce}$ and $1/2f_{ceq}$ are in both cases very close to each other with respect to the frequency resolution of the frequency channels. Magenta dots represent the upper frequency cutoffs of the lower band, black dots show the lower frequency cutoffs of it. For the upper band, gray dots give the upper frequency cutoffs and brown dots represent lower frequency cutoffs. Note that the plots seem to show several black dots at different frequencies for a given time. There is, however, just one dot at each time, and the combination of the size of the plotting symbols and the time resolution of the figure makes them look as a continuous lines. The same note concerns also the magenta dots.

4. Results of a Statistical Study

Figure 3a shows the orbital coverage of the measurements of the STAFF-DWP instrument on board the TC-1 spacecraft from the beginning of January 2004 till the end of September 2007, representing 28,206 h of data. This number of hours correspond to all available data from the STAFF-DWP instrument on board TC-1 spacecraft. We did not exclude time intervals where STAFF-DWP measurements were affected by the interferences, because their amount was negligible with respect to the total amount of data when the measurements from the STAFF-DWP instrument were available. The coverage of all TC-1 orbits is given in a polar plot represented by MLT and L shell. The number of hours of the instrument operation is given in each bin (1 h of MLT × 1 L shell). Square diagrams in Figures 3b and 3c, respectively, show the number of hours of TC-1 (STAFF-DWP instrument) measurements in bins of 4° × 0.5 (magnetic dipole latitude λ_m × L shell) and in bins of 4° × 1 h (λ_m × MLT). All TC-1 orbits cover a wide interval of L shells (2–12), and all MLT sectors at $\lambda_m > 0$, while at $\lambda_m < 0$ they mainly cover dayside MLT. The percentage of time intervals of the preselected BE events from the preliminary list is shown in a polar L−MLT plot (Figure 3d) and square $\lambda_m - L$ and λ_m−MLT diagrams in Figures 3e and 3f, respectively. Occurrence rates of preselected intervals containing chorus-like BEs correspond to hours of observations of these emissions in a given bin divided by the number of hours spent by the TC-1 in this particular bin. It is evident that selected intervals from the preliminary list containing chorus-like BEs were mainly found from the postmidnight to the postnoon magnetic local times (MLT: 1–14), and that they correspond to > 20% of all TC-1 orbits in these bins. Selected intervals from the list containing BEs cover the entire λ_m range from −30° to 30°. The same procedure used for the calculation of the occurrence rate of preselected intervals from the list was also used for the calculation of the occurrence rates of the lower band and of the upper band emissions that were identified by the automatic procedure. The occurrence rates for the lower band are shown in Figures 3g–3i and for the upper band are given in Figures 3j–3l. The lower band intervals covered 297 h of data but the upper band intervals covered only 23 h. Both bands were simultaneously observed only during 11 h. The lower band covered much wider interval of λ_m (from −30° to 30° on the dayside) than the upper band which was concentrated within 10° of λ_m . The lower band was found in a broader MLT interval and also in a broader interval of L values (4–12), while the upper band was primarily concentrated closer to the Earth and on the dawnside.

Average power spectral density, PSD ($nT^2\ Hz^{-1}$), average frequency bandwidth, BW (Hz), and average amplitude A (pT) of the lower band are shown in Figures 4a–4c. The same variables as in Figures 4a–4c but for the upper band events are shown in Figures 4d–4f. The magnitude of PSD of the lower band is on average by 1.5 orders of magnitude larger than the PSD of the upper band. The maximum of the lower

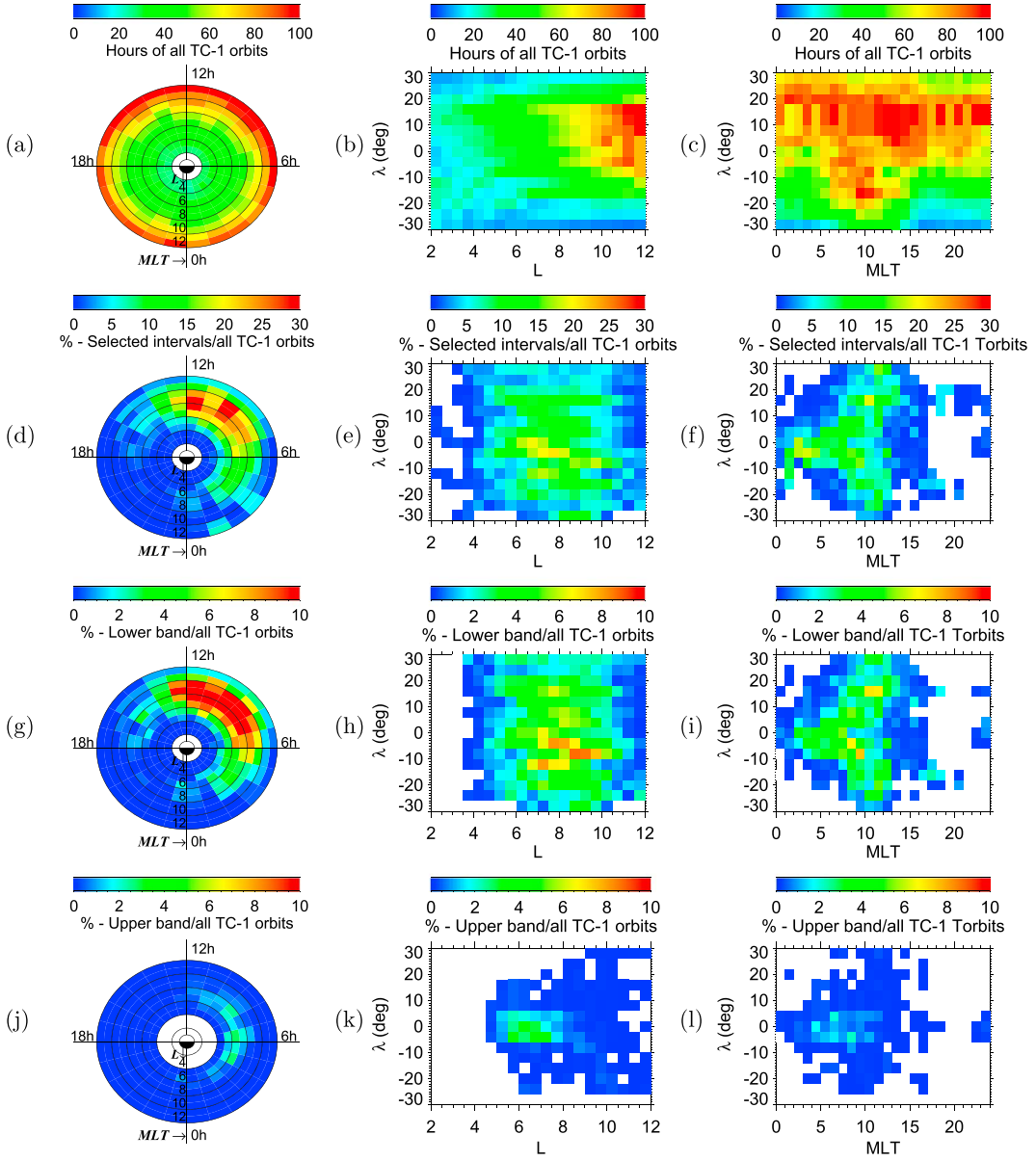

Figure 3. (a, d, g, and j) Polar plots represented by the magnetic local time (MLT) and the L shell, where one bin is 1 MLT × 1 L shell; (b, e, h, and k) square diagrams represented by magnetic latitude (λ_m) and the L shell with one bin given as 4° λ_m × 1 L shell, and (c, f, i, and l) square diagrams λ_m-MLT with one bin 4° λ_m × 1 h of MLT. Figures 3a–3c are numbers of hours calculated from all TC-1 orbits that the spacecraft spent in given bins, Figures 3d–3f are the percentage of hours of time intervals from the list containing BEs preselected for further processing, Figures 3g–3i are the occurrence rate of automatically identified lower band emissions, and Figures 3j–3l are the occurrence rate of automatically identified upper band emissions.

band BW (more than 1 kHz) was found at MLT from 5 to 18, on the other hand the highest values of BW (700–800 Hz) of the upper band was observed from 0 to 13 h of MLT. The maximum values of the BW of lower as well as of upper bands were found close to the Earth.

Lower band BE with average amplitudes >80 pT was detected from premidnight to prenoon at $L = 3$–10. The upper band with amplitudes >80 pT was observed from the midnight to 8 h MLT but much closer to the Earth ($L \leq 6$). The overall average value of amplitude of the lower band emissions across the entire L interval and all MLT sectors is 57 pT and of the upper band is around 20 pT.

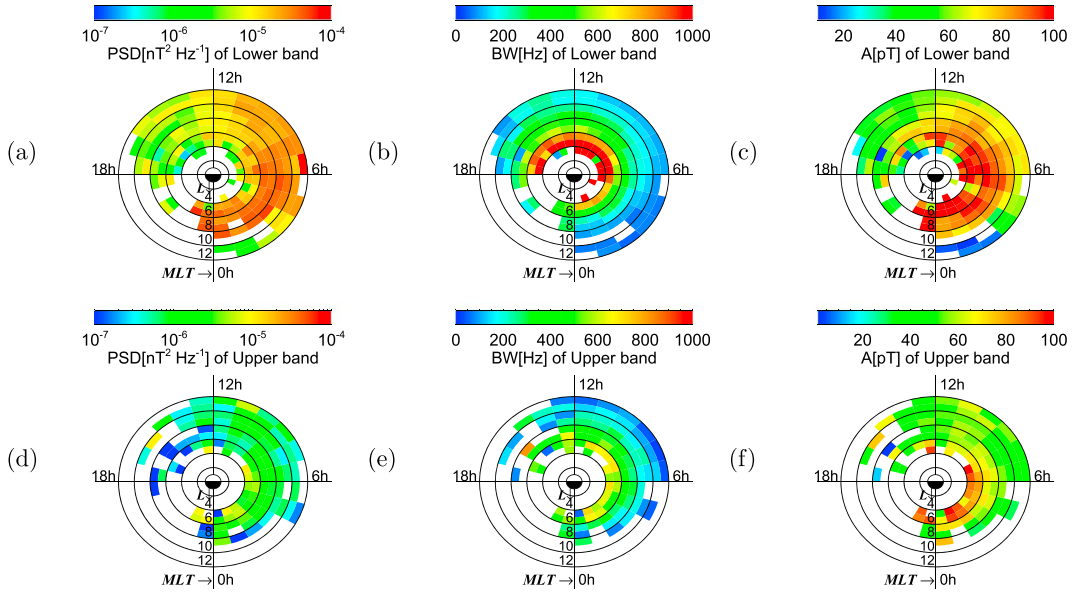

Figure 4. Polar plots as a function of MLT and L shell with the same bins as in Figures 3a–3d, (a) average value of PSD (nT^2 Hz^{-1}) of identified lower band emissions (below $1/2f_{ceq}$), (b) their frequency bandwidth (BW) (Hz), (c) their amplitude (pT), and (d)–(f) the same polar plots as in Figures 4a–4c but for the upper band emissions (above $1/2f_{ceq}$) identified by the automatic procedure.

Variations of PSD, bandwidth, amplitudes, and occurrence rates of the lower and the upper bands under different geomagnetic conditions are shown in Figures 5 and 6. These variations are more pronounced for the lower band than for the upper band. It is clearly visible in two following figures (Figures 5 and 6). Figures 5a, 5d, 5g, 5j, 6a, 6d, 6g, and 6j correspond to quiet geomagnetic conditions ($0 < AE(nT) \leq 100$), Figures 5b, 5e, 5h, 5k, 6b, 6e, 6h, and 6k show results for moderate geomagnetic conditions ($100 < AE(nT) \leq 300$), and Figures 5c, 5f, 5i, 5l, 6c, 6f, 6i, and 6l correspond to disturbed geomagnetic conditions ($AE(nT) > 300$). Plots of f_{ceq} for all levels of geomagnetic activity are in Figures 6m–6o. During quiet geomagnetic conditions the overall average amplitude of lower band BE is 39 pT and for the upper band BE is 13 pT. Maximum value of the amplitude of the lower band is below 400 pT, and 5% of events have amplitude greater than 100 pT for quiet geomagnetic conditions. For the upper band it is below 100 pT, and only 1% of events have amplitude larger than 50 pT. During moderate geomagnetic conditions the overall average amplitude is 55 pT for the lower band and 17 pT for the upper band. Almost 13% of time points (each time interval lasting 4 s) from the lower band BE have amplitude larger than 100 pT, and 5% of time points from the upper band have amplitude larger than 50 pT. The overall average value of amplitude of the lower band during disturbed geomagnetic conditions is 76 pT, and for the upper band it is 24 pT. Several thousand time points (26%) from lower band have amplitude > 100 pT, but only several hundred time points (10%) from upper band have $A > 50$ pT during disturbed geomagnetic conditions. The magnitude of average amplitude (Figure 5) therefore significantly increases with increasing geomagnetic activity for the lower band emissions.

Average values of PSD, amplitudes, and occurrence rates of lower band emissions are one and a half times greater for active conditions than for quiet conditions, but the increase of PSD for the upper band is almost negligible. During quiet conditions the largest values of PSDs and amplitudes of the lower band BE are concentrated within 10° of λ_m, but they are extended toward larger magnetic latitudes during moderate and disturbed geomagnetic conditions. Both occurrence rates for the lower band and for the upper band increase in L shell region between 5 and 9 with increasing activity. The increase of PSD, BW, and A values is much less significant for the upper band than for the lower band. Only the average occurrence rate of the upper band between $L = 4$ and $L = 8$ and within $\lambda_m = 10°$ is 2 times larger during active geomagnetic conditions than during quiet geomagnetic conditions. The upper band emission covers almost the same

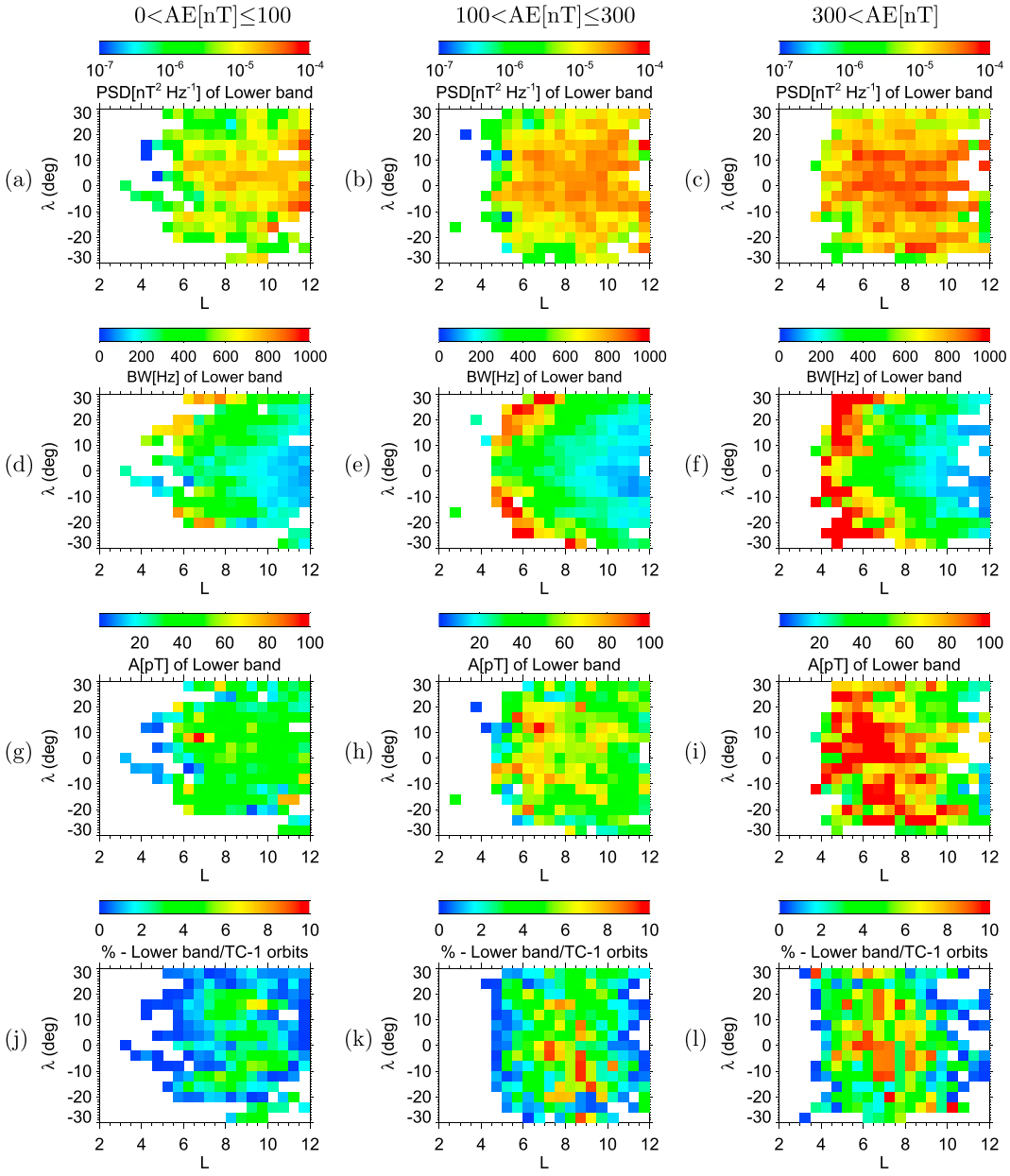

Figure 5. (a) Average PSD, (d) average bandwidth, (g) average amplitude, and (j) occurrence rate for automatically identified lower band emissions represented as a function of λ_m and L shell for quiet geomagnetic conditions ($0 < AE(\mathrm{nT}) \leq 100$), (b, e, h, and k) the same for moderate geomagnetic conditions ($100 < AE(\mathrm{nT}) \leq 300$), and (c, f, i, and l) for active geomagnetic conditions, where *AE* is larger than 300 nT.

interval of λ_m for all levels of the geomagnetic activity. These results may be consistent with theoretical assumptions [*Omura et al.*, 2009] and based on the Geotail measurements [*Habagishi et al.*, 2014].

Figures 7 and 8 show the properties of the lower and upper band emissions in two MLT sector of their maximum occurrence. Figure 7 presents values of PSD, BW, and amplitude for the dawnside MLT sector (3–9). The most intense (with larger values of PSD) dawnside lower band emissions are mainly concentrated at low and middle magnetic latitudes ($\lambda_m \leq 20°$), while the intense dawnside upper band events are found within smaller interval of magnetic latitudes (−10°, 10°). The same effect is also evident for the amplitude of the nightside lower band emissions. Lower band emissions with amplitudes ≥100 pT (the average amplitude of the lower band is 67 pT) are located within 25° of λ_m and at $L \leq 10$, while the upper band BEs

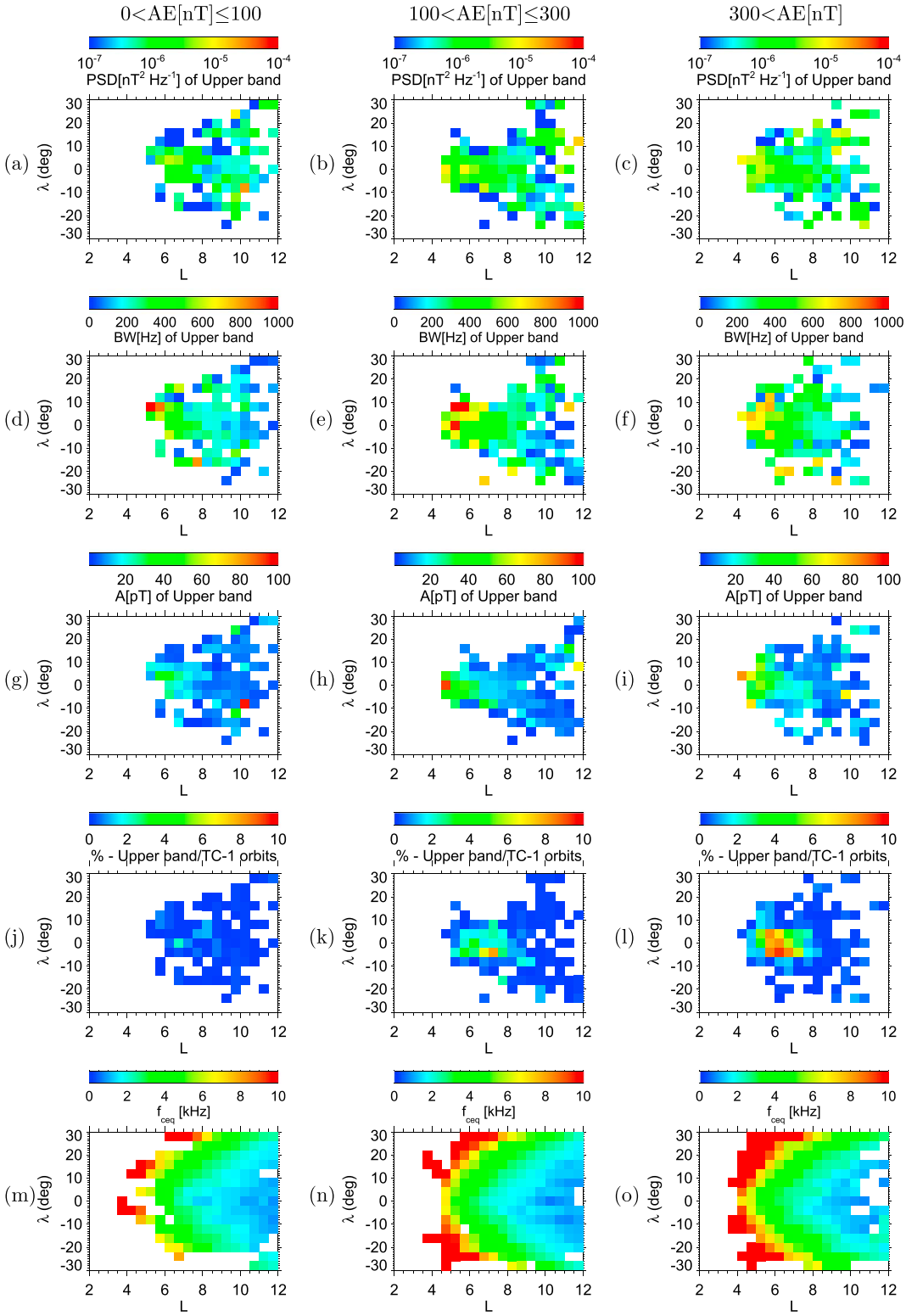

Figure 6. (a–l) The same set of plots as in Figure 5 but for upper band emissions identified by an automatic procedure. (m–o) The evolution of the f_{ceq} under different geomagnetic conditions as a function of λ_m and L shell.

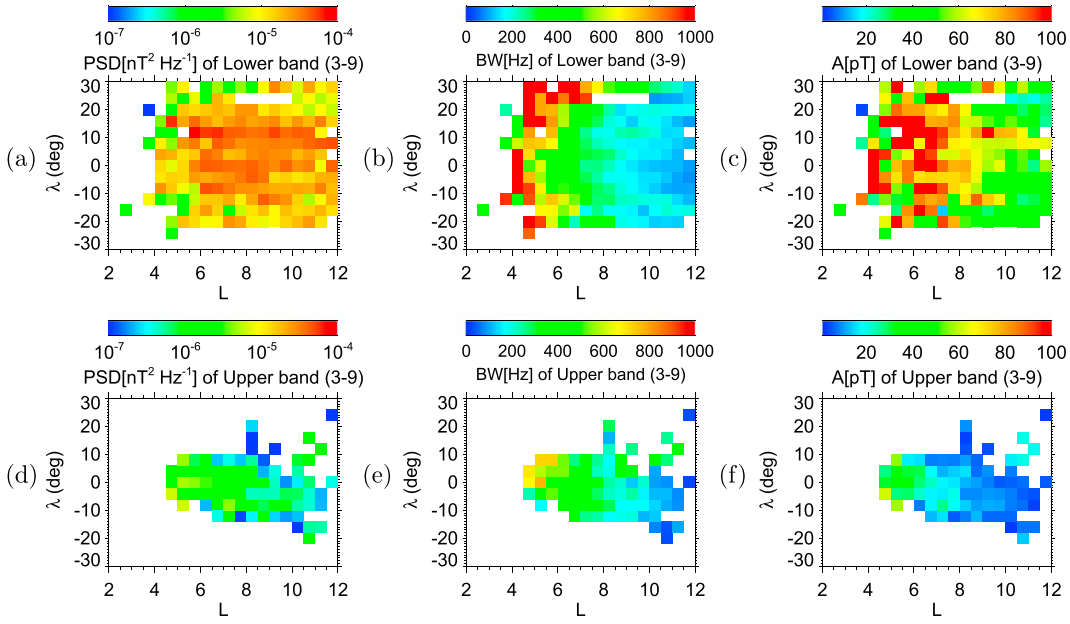

Figure 7. (a) Average PSD, (b) average bandwidth, and (c) average amplitude of all identified dawnside lower band emissions (MLT: 3–9), (d–f) the same set of plot as in Figures 7a–7c but for the identified dawnside upper band emissions at MLT between 3 and 9 h.

with amplitudes ≥50 pT (the average amplitude = 21 pT) were found close to the geomagnetic equator (≤10°) and at $L \leq 7$. Both the dayside (MLT 9–15) lower band emissions with the average amplitude of 50 pT and the upper band emissions (average amplitude =13 pT) are less intense than the dawnside emissions. The frequency bandwidths of the lower and the upper bands of the dayside emissions are slightly larger than those of dawnside emissions. We can see that amplitudes of the dayside lower band emissions increase with increasing λ_m. The lower band emissions with amplitudes >100 pT were measured only up to $L = 7.5$. There is just several time points from the dayside upper band emissions with amplitudes larger than 50 pT. The duskside lower and upper bands (not shown) were found mainly at middle magnetic

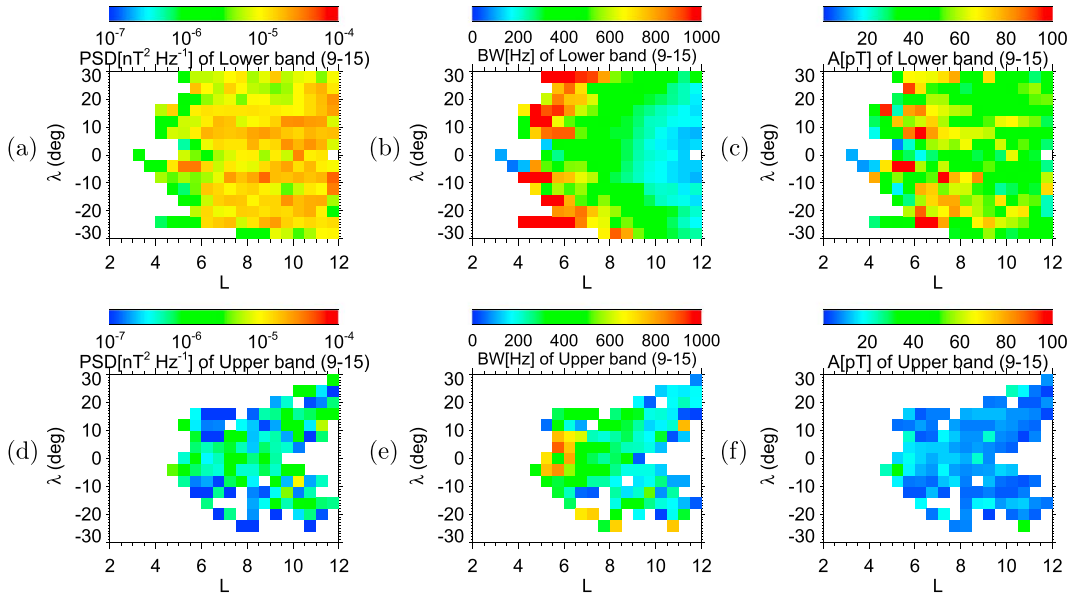

Figure 8. (a) Average PSD, (b) average bandwidth, and (c) average amplitude of all identified dayside lower band emissions at MLT between 9 and 15 h. (d–f) The same set of plot as in Figures 8a–8c but for the identified dayside upper band emissions (MLT: 9–15).

latitudes. Emissions at the geomagnetic equator on the duskside were not found, while the nightside emissions (not shown) were concentrated close to the geomagnetic equator ($\lambda_m < 10°$ for lower band and $\lambda_m < 5°$ for upper band). The average values of amplitudes of duskside lower and upper band emissions are, respectively, equal to 33 pT and to 9 pT, while the average values of amplitudes of the nightside lower and upper band observed are 61 pT and 39 pT, respectively.

5. Discussion

We have identified all observed chorus-like banded events by using wave measurements from the entire operational period of the *Double Star* TC-1 spacecraft (beginning of January 2004 to end of September 2007). The equatorial orbit of the spacecraft caused that all observed events were localized within 30° of magnetic latitude (λ_m). We were unable to resolve the inner fine structure of banded emission from the power spectrograms, owing to a limited time resolution (4 s) of the onboard calculated spectra. Selected time intervals of banded emissions were found in more than 20% of all TC-1 orbits, mostly in the dawnside and dayside MLT sectors and at L values from 6 to 11. It agrees with the area where injected electrons can excite whistler-mode waves during their drift from the nightside through the dawnside toward the noon sector. The obtained occurrence rates might be slightly underestimated because we exclude intervals where the power spectral density of band-limited whistler-mode emissions is less than 2 orders of magnitude above the background.

All these time intervals with BE that satisfied predefined selection criteria were subsequently processed by a computer procedure that identified the lower band and the upper band emissions and determined their BW, PSD, and amplitude. This procedure determines the frequency bandwidths of both chorus bands using the measured spectra. This is different from previous studies where assumption of fixed bandwidths for the lower and the upper bands was used to transform the measured power spectral densities into wave amplitudes [e.g., *Li et al.*, 2011a; *Meredith et al.*, 2012]. The frequency interval for the lower band was assumed to be 0.1–0.5 f_{ce} in both of these studies, and frequency interval for the upper band was assumed to be 0.5–0.8 f_{ce} [*Li et al.*, 2011a] or 0.5–1 f_{ce} [*Meredith et al.*, 2012]. After normalizing our results from Figures 4b and 4e by the electron cyclotron frequency (not shown), they generally indicate lower average normalized bandwidths: 0.1–0.3 f_{ce} for the lower band and 0.5–0.7 f_{ce} for the upper band.

To verify the robustness of these results, we have varied the threshold value (0.05) from the condition 2 between 0.01 and 0.1. This variation has only small influence on the accuracy of the BE detection on the global scale and a negligible influence on the final results. The largest threshold value (0.1) caused the decrease of BW (by approximately 10% on average). The lowest threshold value (0.01) had an opposite effect on BW. The BW value has increased by approximately 10% on average. The decrease and increase of BW were much stronger for the lower band (its lower cutoff varied by ~7% and its upper cutoff varied by ~11%) than for the upper band (where both cutoffs varied by ~5%). These variations were most evident between 12 and 18 h MLT at $L < 6$. The resulting variations of the amplitude were negligible. When the procedure has detected a larger BW, it has also detected parts of the background. It means that the average PSD value was slightly smaller; therefore, the amplitude almost did not change. The same situation but with the opposite effect was observed when we have used the largest threshold values.

The lower band was observed much more frequently and in a wider interval of λ_m from −30° to 30° and of L shells (4–11) than the upper band which was mostly localized within 10° of λ_m and at lower L values. The generation of the upper band is probably given by the higher anisotropy of resonant electrons which is preferentially present at lower L shell [*Kennel and Petschek*, 1966; *Li et al.*, 2010]. The lower band was most often found in the dawnside and dayside MLT sectors, while the upper band was mainly seen on the dawnside. This is in agreement with results which have been previously published by *Santolik et al.* [2005a] and *Meredith et al.* [2012]. Compared to the study by *Santolik et al.* [2005a] which uses the data from the same TC-1 spacecraft, we have, in the present work, used a much larger data set covering the whole operational period of the mission. Our results are in agreement with those of *Santolik et al.* [2005a] and *Meredith et al.* [2012].

The PSD of the lower band events are by 1 order of magnitude greater than the PSD of the upper band, while average amplitude of lower band is almost 3 times larger than the average amplitude of the upper band (similar as in the paper by *Li et al.* [2011a]). The overall average amplitude of the lower band is 57 pT and of the upper band is approximately 20 pT.

The PSD, the amplitude of the lower band, its frequency bandwidth, and its occurrence rate significantly increase with increasing geomagnetic activity. Large amplitude lower band emissions cover a wider interval of λ_m during active geomagnetic conditions than during quiet conditions, while the intense upper band emissions cover almost the same interval of λ_m for all levels of geomagnetic activity. This may be consistent with conclusions of *Omura et al.* [2009] and *Habagishi et al.* [2014]. We found more than 14% of time points from the lower band with amplitudes larger than 100 pT and more than 6% from the upper band with amplitudes larger than 50 pT. The largest amplitudes of lower band emissions were found in the nightside and in the dawnside MLT sector, but the most intense upper band emissions were observed mainly on the nightside. On the other hand, variations of PSD, BW, and amplitude of the upper band do not significantly depend on the geomagnetic activity. The occurrence rate of upper band emissions is the only parameter which increases with the increasing geomagnetic activity. It is 2 times larger for active geomagnetic conditions than for quiet conditions. Different dependence of the lower and the upper band on the geomagnetic activity can be connected with different resonant energies of energetic electrons that are responsible for the generation of different frequencies of chorus. The upper band chorus interacts with electrons that have small resonant energies, typically between 500 eV and a few keV. The resonant energies of energetic electrons resonating with the lower band chorus are larger (>10 keV) [*Li et al.*, 2010]. Different behavior of the lower and the upper bands of chorus therefore can mean that properties of their source electron distributions are differently linked to increases of the geomagnetic activity, becoming more unstable at larger energies.

PSD, BW, amplitude, and occurrence rate also depend on MLT. For the nightside and dawnside MLT sectors, the largest values of these parameters are confined to low latitudes. The amplitude of banded emissions (both bands) in these MLT sectors is higher than in the other MLT sectors. Dayside (at $L < 8$) and duskside lower and upper band emissions occur more often at middle magnetic latitudes ($\lambda_m > 10°$) than around the geomagnetic equator. The increase of amplitude with λ_m is most noticeable on the dayside. The average amplitude of the lower band is smaller on the duskside than on the nighsite or dayside. These two factors can cause that some duskside BEs observed close to the equator have a similar level of intensity as the background. Therefore, we can expect that the recognition procedure did not identify all weak events. It can be one of reasons why we have observed smaller occurrence rate close to the geomagnetic equator than at larger geomagnetic latitudes ($\lambda_m > 10°$). The same effect but not so strong was found at $L < 8$ on the dayside. The occurrence rates of BE did not depend on the λ_m in other MLT sectors.

Dayside and nightside lower band emissions with amplitudes >100 pT are found in a broader region of L shells than in the other MLT sectors, where they are mostly localized closer to the Earth.

6. Conclusion

Our statistical study of chorus-like banded emissions is based on a unique automated detection of their lower and upper frequency limits using the data of the STAFF-DWP instrument on board the equatorial *Double Star* spacecraft. Unlike previous studies which rely on assumptions about the frequency band of these emissions, our procedure allows us to estimate the bandwidths and amplitudes of chorus-like emissions and their dependencies on magnetic local time, magnetic latitude, L shell, and on geomagnetic activity.

1. We observe large amplitude (>100 pT) emissions mainly on the nightside and on the dawnside. They are confined close to the geomagnetic equator and occur up to $L = 10$. Intense dayside and duskside emissions cover a larger area of magnetic latitudes.
2. Automatically detected chorus-like emissions were found with the highest probability mainly on the dayside. The lower band emissions at frequencies below one half of the equatorial electron cyclotron frequency occur 10 times more often than the upper band emissions at higher frequencies. On the other hand, upper band emissions were observed with the largest occurrence rate on the dawnside.
3. Normalized bandwidths of both frequency bands fluctuate around 0.2 f_{ce}. The lower band is on average found between 0.1 f_{ce} and 0.3 f_{ce}, while the upper band was detected from 0.5 f_{ce} to 0.7 f_{ce}.
4. Average amplitudes of the lower band waves are 3 times larger than those of the upper band. The intense lower band emissions also cover a wider interval of L shell and λ_m than intense upper band waves.
5. Power spectral density, frequency bandwidth, and amplitude of the lower band emissions are sensitive to variations of the geomagnetic activity reflected by the *AE* index. Average values of all these parameters

increase with increasing geomagnetic activity. The same parameters describing properties of the upper band vary only slightly with the increasing *AE* index. This effect can be connected with different resonant energies of energetic electrons that are responsible for the generation of the lower and the upper band.

Acknowledgments
This work receives EU support through the FP7-Space grant agreement 284520 for the MAARBLE collaborative research project. This work was also supported by GAUK grant 678212, by Kontakt LH 11122, and by the GACR grants 205/10-2279 and P209-11-2280. The *Double Star* data are distributed by the European Space Agency. The *AE* data are provided by the World Data Center for Geomagnetism, Kyoto (http://wdc.kugi.kyoto-u.ac.jp/).

Yuming Wang thanks Xin Tao and Yoshiharu Omurafor their assistance in evaluating this paper.

References

Bortnik, J., R. M. Thorne, and N. P. Meredith (2008), The unexpected origin of plasmaspheric hiss from discrete chorus emissions, 62–66, doi:10.1038/nature06741.

Burtis, W. J., and R. A. Helliwell (1969), Banded chorus—A new type of VLF radiation observed in the magnetosphere by OGO 1 and OGO 3, *J. Geophys. Res.*, *74*(11), 3002–3010, doi:10.1029/JA074i011p03002.

Burtis, W. J., and R. A. Helliwell (1976), Magnetospheric chorus: Occurrence patterns and normalized frequency, *Planet. Space Sci.*, *24*, 1007–1024.

Chen, L., J. Bortnik, W. Li, R. M. Thorne, and R. B. Horne (2012a), Modeling the properties of plasmaspheric hiss: 1. Dependence on chorus wave emission, *J. Geophys. Res.*, *117*, A05201, doi:10.1029/2011JA017201.

Chen, L., J. Bortnik, W. Li, R. M. Thorne, and R. B. Horne (2012b), Modeling the properties of plasmaspheric hiss: 2. Dependence on the plasma density distribution, *J. Geophys. Res.*, *117*, A05202, doi:10.1029/2011JA017202.

Chum, J., and O. Santolík (2005), Propagation of whistler-mode chorus to low altitudes: Divergent ray trajectories and ground accessibility, *Ann. Geophys.*, *23*, 3727–3738, doi:10.5194/angeo-23-3727-2005.

Cornilleau-Wehrlin, N., R Gendrin, F. Lefeuvre, M. Parrot, R. Grard, D. Jones, A. Bahnsen, E. Ungstrup, and W. Gibbons (1978), VLF electromagnetic waves observed onboard GEOS-1, *Space Sci. Rev.*, *22*, 371–382.

Cornilleau-Wehrlin, N., et al. (2005), The STAFF-DWP wave instrument on the DSP equatorial spacecraft: Description and first results, *Ann. Geophys.*, *23*, 2785–2801, doi:10.5194/angeo-23-2785-2005.

Escoubet, C. P., Z.-X. Liu, and Z. Pu (2005), Double star—First results, *Ann. Geophys.*, *23*, 2705–2705.

Habagishi, T., S. Yagitani, and Y. Omura (2014), Nonlinear damping of chorus emissions at local half cyclotron frequencies observed by Geotail at L > 9, *J. Geophys. Res. Space Physics*, *119*, 4475–4483, doi:10.1002/2013JA019696.

Haque, N., U. S. Inan, T. F. Bell, and J. S. Pickett (2012), Spatial dependence of banded chorus intensity near the magnetic equator, *Geophys. Res. Lett.*, *39*, L17103, doi:10.1029/2012GL052929.

Katoh, Y., and Y. Omura (2007), Computer simulation of chorus wave generation in the Earth's inner magnetosphere, *Geophys. Res. Lett.*, *34*, L03102, doi:10.1029/2006GL028594.

Katoh, Y., and Y. Omura (2011), Amplitude dependence of frequency sweep rates of whistler mode chorus emissions, *J. Geophys. Res.*, *116*, A07201, doi:10.1029/2011JA016496.

Kennel, C. F., and H. E. Petschek (1966), Limit on stable trapped particle fluxes, *J. Geophys. Res.*, *71*, 1–28.

Kurita, S., Y. Katoh, Y. Omura, V. Angelopoulos, C. M. Cully, O. Le Contel, and H. Misawa (2012), THEMIS observation of chorus elements without a gap at half the gyrofrequency, *J. Geophys. Res.*, *117*, A11223, doi:10.1029/2012JA018076.

LeDocq, M. J., D. A. Gurnett, and G. B. Hospodarsky (1998), Chorus source locations from VLF Poynting flux measurements with the Polar spacecraft, *Geophys. Res. Lett.*, *25*, 4063–4066, doi:10.1029/1998GL900071.

Li, W., R. M. Thorne, V. Angelopoulos, J. Bortnik, C. M. Cully, B. Ni, O. LeContel, A. Roux, U. Auster, and W. Magnes (2009), Global distribution of whistler-mode chorus waves observed on the THEMIS spacecraft, *Geophys. Res. Lett.*, *36*, L09104, doi:10.1029/2009GL037595.

Li, W., et al. (2010), THEMIS analysis of observed equatorial electron distributions responsible for the chorus excitation, *J. Geophys. Res.*, *115*, A00F11, doi:10.1029/2009JA014845.

Li, W., J. Bortnik, R. M. Thorne, and V. Angelopoulos (2011a), Global distribution of wave amplitudes and wave normal angles of chorus waves using THEMIS wave observations, *J. Geophys. Res.*, *116*, A12205, doi:10.1029/2011JA017035.

Li, W., R. M. Thorne, J. Bortnik, Y. Y. Shprits, Y. Nishimura, V. Angelopoulos, C. Chaston, O. Le Contel, and J. W. Bonnell (2011b), Typical properties of rising and falling tone chorus waves, *Geophys. Res. Lett.*, *38*, L14103, doi:10.1029/2011GL047925.

Macúšová, E., and O. Santolík (2009), Database of whistler-mode chorus in the equatorial plane, in *WDS'09 Proceedings of Contributed Papers: Part II—Physics of Plasmas and Ionized Media*, edited by J. Safrankova and J. Pavlu, pp. 56–61, Matfyzpress, Prague, Czech Republic.

Meredith, N. P., R. B. Horne, A. Sicard-Piet, D. Bosher, K. H. Yearby, W. Li, and R. M. Thorne (2012), Global model of lower band and upper band chorus from multiple satellite observations, *J. Geophys. Res.*, *117*, A10225, doi:10.1029/2012JA017978.

Ni, B., R. M. Thorne, Y. Y. Shprit s, and J. Bortnik (2008), Resonant scattering of plasma sheet electrons by whistler-mode chorus: Contribution to diffuse auroral precipitation, *Geophys. Res. Lett.*, *35*, L11106, doi:10.1029/2008GL034032.

Nishimura, Y., et al. (2010), Identifying the driver of the pulsating aurora, *Science*, *330*, 81–84, doi:10.1126/science.1193186.

Omura, Y., M. Hikishima, Y. Katoh, D. Summers, and S. Yagitani (2009), Nonlinear mechanisms of lower-band and upper-band VLF chorus emissions in the magnetosphere, *J. Geophys. Res.*, *114*, A07217, doi:10.1029/2009JA014206.

Parrot, M., O. Santolík, N. Cornilleau-Wehrlin, M. Maksimovic, and C. C. Harvey (2003), Source location of chorus emissions observed by Cluster, *Ann. Geophys.*, *21*, 473–480, doi:10.5194/angeo-21-473-2003.

Santolik, O., and D. A. Gurnett (2003), Transverse dimensions of chorus in the source region, *Geophys. Res. Lett.*, *30*(2), 1031, doi:10.1029/2002GL016178.

Santolik, O., M. Parrot, and F. Lefeuvre (2003), Singular value decomposition methods for wave propagation analysis, *Radio Sci.*, *38*(1), 1010, doi:10.1029/2000RS002523.

Santolik, O., D. A. Gurnett, and J. S. Pickett (2004), Multipoint investigation of the source region of storm-time chorus, *Ann. Geophys.*, *22*, 2552–2563.

Santolik, O., D. A. Gurnett, J. S. Pickett, M. Parrot, and N. Cornilleau-Wehrlin (2005a), Central position of the source region of storm-time chorus, *Planet. Space Sci.*, *53*, 299–305.

Santolik, O., E. Macusova, K. H. Yearby, N. Cornilleau-Wehrlin, and H. S. K. Alleyne (2005b), Radial variation of whistler-mode chorus: First results from the STAFF/DWP instrument on board the Double Star TC-1 spacecraft, *Ann. Geophys.*, *23*, 2937–2942, doi:10.5194/angeo-23-2937-2005.

Santolik, O., D. A. Gurnett, J. Pickett, and N. Cornilleau-Wehrlin (2006), Five years of investigation of whistler-mode chorus using the measurements of the Cluster spacefleet, in *Proceedings of Cluster and Double Star Symposium 5th Anniversary of Cluster in Space*, edited by K. Fletcher, pp. 1–8, ESA Publ. Div., Noordwijk, Netherlands.

Santolik, O., D. A. Gurnett, J. S. Pickett, J. Chum, and N. Cornilleau-Wehrlin (2009), Oblique propagation of whistler mode waves in the chorus source region, *J. Geophys. Res.*, *114*, A00F03, doi:10.1029/2009JA014586.

Sazhin, S. S., and M. Hayakawa (1992), Magnetospheric chorus emissions: A review, *Planet. Space Sci.*, *40*, 681–697.

Tao, X., J. Bortnik, R. M. Thorne, J. M. Albert, and W. Li (2012), Effects of amplitude modulation on nonlinear interactions between electrons and chorus waves, *Geophys. Res. Lett.*, *39*, L06102, doi:10.1029/2012GL051202.

Thorne, R. M., B. Ni, X. Tao, R. M. Thorne, and N. P. Meredith (2010), Scattering by chorus waves as the dominant cause of diffuse auroral precipitation, *Nature*, *467*, 943–946, doi:10.1038/nature09467.

Thorne, R. M., et al. (2013), Rapid local acceleration of relativistic radiation-belt electrons by magnetospheric chorus, *Nature*, *504*, 411–420, doi:10.1038/nature12889.

Tsurutani, B. T., and E. J. Smith (1974), Postmidnight chorus: A substorm phenomenon, *J. Geophys. Res.*, *79*, 118–127.

Tsurutani, B. T., and E. J. Smith (1977), Two types of magnetospheric ELF chorus and their substorm dependences, *J. Geophys. Res.*, *82*, 5112–5128.

Yagitani, S., T. Habagishi, and Y. Omura (2014), Geotail observation of upper band and lower band chorus elements in the outer magnetosphere, *J. Geophys. Res. Space Physics*, *119*, 4694–4705, doi:10.1002/2013JA019678.